Magnetism and site occupancy in epitaxial Y-rich yttrium iron garnet films

Tingyu Su [1,*] Shuai Ning [2,3,†] Eunsoo Cho,[2] and Caroline A. Ross [2,‡]

[1]*Department of Mechanical Engineering, Massachusetts Institute of Technology, Cambridge, Massachusetts 02139, USA*

[2]*Department of Materials Science and Engineering, Massachusetts Institute of Technology, Cambridge, Massachusetts 02139, USA*

[3]*School of Materials Science and Engineering, National Institute for Advanced Materials, Nankai University, Tianjin, 300350, People's Republic of China*

(Received 10 May 2021; revised 14 August 2021; accepted 17 August 2021; published 8 September 2021)

Y-rich yttrium iron garnet (Y-YIG) thin films were grown on gadolinium gallium garnet substrates using pulsed laser deposition from a $YFeO_3$ target. The films are epitaxial on the substrate, and the unit cell of (001)- and (111)-oriented Y-YIG undergoes a tetragonal or rhombohedral distortion, respectively. The Y-YIG has lower room temperature magnetization but higher low-temperature magnetization than bulk YIG, and its Curie temperature was in the range of 330–400 K, depending on the growth conditions. First-principles calculations predict that Y_{Fe} antisite defects are more stable in octahedral than tetrahedral Fe sites. Temperature-dependent magnetization measurements together with a superexchange dilution model and composition determined from x-ray photoelectron spectroscopy indicate that nonmagnetic species (Y^{3+} and vacancies) are predominantly accommodated in the octahedral sites, but there is a significant occupancy of tetrahedral sites.

DOI: 10.1103/PhysRevMaterials.5.094403

I. INTRODUCTION

Yttrium iron garnet (YIG, $Y_3Fe_2Fe_3O_{12}$) has been intensively studied for its useful magnetic and magnetic-optical properties [1–3]. The garnet structure comprises three cation sites, dodecahedral (*c* sites), octahedral (*a* sites), and tetrahedral (*d* sites), which in YIG are occupied by Y^{3+}, Fe^{3+}, and Fe^{3+}, respectively. These sites may be occupied by many different cations to form stable garnets that exhibit a wide range of electronic properties. For example, Gilleo and Geller [4] and Geller *et al.* [5,6]showed that Al^{3+}, In^{3+}, Sc^{3+}, Ni^{2+}, Mn^{2+}, Si^{4+}, Ge^{4+}, Ca^{2+}, and Co^{2+} can substitute for the *a*- or *d*-site Fe^{3+} in YIG, forming ferrimagnetic garnets with a range of magnetic moments, Curie temperatures, and other properties. The lattice parameter and magnetization vs temperature of $Y_3Fe_{5-x}M_xO_{12}$ ($M = In^{3+}$, Sc^{3+}, Al^{3+}, or Ga^{3+}) depend on the amount of substitution x and which Fe^{3+} site is occupied by the substituent [3]. Furthermore, the (*c*-site) Y^{3+} can be partially or completely replaced by rare earth ions such as Gd, Sm, Eu, Tb, Lu, Ho, Tm, or Dy, allowing the anisotropy, magnetostriction, compensation temperature, and magnetization to be varied [7–9], or by Ce^{3+} or Bi^{3+}, forming Ce:YIG or Bi:YIG with enhanced magneto-optical activity compared with that of YIG [10–14].

The site preference of cations on the *a*, *c*, and *d* sites is primarily governed by their ionic radius, with smaller ions such as Si^{4+} or Al^{3+} preferentially occupying the tetrahedral *d* sites, and larger ions such as rare earths occupying the dodecahedral *c* sites [7,9]. Some substituents show a full range of solid solubility, such as Al, Sm, or Ga in $Y_3Al_xFe_{5-x}O_{12}$ [15], $Y_{3-y}Sm_yFe_5O_{12}$ [16], and $Y_3Fe_{5-x}Ga_xO_{12}$, respectively [17], where $0 \leqslant x \leqslant 5$ and $0 \leqslant y \leqslant 3$, but in other cases, the extent of substitution is limited to a certain level, beyond which a secondary phase will form. For example, for octahedral In^{3+} substitution ($Y_3Fe_{2-x}In_xFe_3O_{12}$), the threshold for a detectable secondary phase [18] is $x = 0.65$, while for Ca^{2+} and Ti^{4+} cosubstitution, the maximum attainable value of x in the single phase garnet [19] $Y_{3-x}Ca_xTi_xFe_{5-x}O_{12}$ is 0.74.

In garnets, the ideal ratio of *c*-site to $a + d$-site cations is 3:5. Deviations from the ideal stoichiometry may be accommodated by the formation of secondary phases or by the presence of antisite defects, vacancies, or other point defects within the garnet lattice. In the case of Y and other rare earth (*R*) garnets, secondary phases include binary oxides of *R* or Fe or *R*,Fe oxides such as the perovskite-structured orthoferrite phase $RFeO_3$. The yttria-iron oxide pseudobinary phase diagram reveals that single phase YIG in air is stable over only a small range of Y:Fe ratios [20], with excess Y leading to a two-phase coexistence of YIG plus $YFeO_3$ and excess Fe leading to coexistence of YIG plus hematite (α-Fe_2O_3) or magnetite (Fe_3O_4) [2,21,22]. Similarly, $Sm_3Fe_5O_{12}$ coexists with $SmFeO_3$ or Fe_2O_3 for excess Sm or excess Fe, respectively [23], and $Eu_3Fe_5O_{12}$ with $EuFeO_3$ or Fe_2O_3 for excess Eu or excess Fe, respectively [24].

These results argue against the formation of significantly Y-rich or Fe-rich YIG when *R*:Fe differs from 0.6. However, the off-stoichiometric garnet phase may be promoted in practice by epitaxial stabilization from a garnet-structured substrate or by nonequilibrium growth methods such as vapor phase deposition. Manuilov *et al.* [25] and Manuilov and Grishin [26] analyzed epitaxial YIG with Y:Fe up to 0.74, explaining the magnetic properties by the presence of Fe vacancies, which preferentially occupy the *a* sites. As another example, epitaxial TbIG films were grown by pulsed laser deposition (PLD) with Tb:Fe = 0.75, and the excess Tb was

*tingyu@mit.edu
†sning@nankai.edu.cn
‡caross@mit.edu

assumed to be accommodated in the *a* sites [27]. Point defects have also been found in polycrystalline YIG, including Fe vacancies in YIG [28–30] and BiYIG [31] films grown at high oxygen pressure and Y_{Fe} antisite defects in YIG [32]. These growth processes and epitaxial stabilization enable the formation of garnet compositions that would not be stable in bulk, offering opportunities for synthesis of materials with diverse magnetic properties.

In this paper, we describe the structure and magnetic properties of epitaxial YIG thin films with a considerable excess Y (Y:Fe ∼ 1:1), a composition that at equilibrium would instead form the orthoferrite phase $YFeO_3$. Our results indicate that the excess Y preferably occupies the octahedral site, though there is also a significant amount of tetrahedral Y and, in some cases, Fe vacancies. The nonmagnetic Fe-site point defects dilute the magnetic exchange coupling between the octahedral and tetrahedral Fe sublattices and lower the Curie temperature and the room-temperature magnetic moment of the Y-rich YIG but raise the low-temperature moment. We use a superexchange dilution model to explain the magnetic temperature dependence of magnetization of Y-rich YIG and compare the properties to those of YIG with other *a*-site substituents.

II. EXPERIMENTAL METHODS

Epitaxial garnet films were grown on gadolinium gallium garnet (GGG) substrates with (001) and (111) orientations by pulsed laser ablation of a $YFeO_3$ (YFO) target or a $Y_3Fe_5O_{12}$ (YIG) target. During growth, the temperature at the backside of the substrate holder was maintained at $T_{sub} = 900\,^{\circ}C$, with the substrate itself ∼150 °C cooler than T_{sub}. The laser was operated at a wavelength of 248 nm with repetition rate of 5 Hz. The oxygen vacancy concentration and cation stoichiometry of PLD-grown thin films are significantly affected by the growth conditions during deposition [33]. In this paper, samples were grown under O_2 pressures of 10 or 150 mTorr and laser power of 300–400 mJ/pulse (fluence of 2.0–2.55 J/cm^2).

Table I summarizes six Y-rich YIG samples analyzed in this paper, and Tables S1 and S2 in the Supplemental Material [34] summarize these and additional samples. High-resolution x-ray diffraction (HRXRD) and asymmetric reciprocal space mapping (RSM) were performed on SmartLab and Bruker D8 diffractometers with Cu $K_{\alpha 1}$ radiation ($\lambda = 1.5406$ Å) and an incident beam Ge-(220) double-bounce monochromator. Thickness was measured by x-ray reflectometry (XRR) and surface roughness by Cypher atomic force microscopy (AFM). Magnetic hysteresis loops at temperatures of 10–400 K were measured using a superconducting quantum interference device (SQUID) magnetometer and a vibrating sample magnetometer, subtracting the GGG background signals using a linear fit. X-ray magnetic circular dichroism (XMCD) at the Fe $L_{2,3}$ absorption edge was collected in total fluorescence yield mode using the beamline 4-ID-C of the Advanced Photon Source at Argonne National Laboratory at 160 K under a magnetic field $H = 5000$ Oe. X-ray photoelectron spectra (XPS) were collected on a PHI Versaprobe II for composition analysis.

Density functional theory (DFT) calculations were performed with the Vienna *Ab initio* Simulation Package (VASP). The Perdew-Burke-Ernzerhof functional was used. The core-valence configurations were Y ($4s^2 4p^6 4d^1 5s^2$), Fe ($3p^6 3d^7 4s^1$), and O ($2s^2 2p^4$). The effective U for the GGA + U method was 5.3 eV for Fe. The energy cutoff was 500 eV, and k-point grids were maintained to a Monkhorst-Pack $2 \times 2 \times 2$ mesh. All calculations were performed in a garnet unit cell that contains 8 formula units (f.u.) of $Y_3Fe_5O_{12}$, and structural characterization was performed using VESTA [35].

III. RESULTS AND DISCUSSION

A. Structure and composition analysis

HRXRD 2θ-ω scans were used to determine the structure and phase of the as-grown films on (001)- and (111)-oriented GGG substrates. Full-range scans ($2\theta = 15$–80°) showed only garnet peaks from the substrate and film, Fig. 1(c) with no orthoferrite peaks. Scans around the primary substrate peaks [Figs. 1(a) and 1(b)] reveal that, compared with YIG films, the Y-YIG samples have a larger out-of-plane lattice spacing, greater than that of YIG by 2.5% and 2.7% for the 67-nm-thick (001) and (111) samples, respectively. The lattice spacing was higher for the thicker films which were formed at a higher growth rate.

The in-plane structural information of Y-YIG films was extracted from the RSMs of asymmetric diffraction peaks.

TABLE I. Summary of Y-YIG samples.

	Growth condition			Structure				Magnetism			Composition			
Samples	O_2 (mTorr)	Laser (mJ)	Rate (nm/h)	Thickness (t) (nm)	$\Delta d/d$[a] (%)	β[b] (deg.)	α[c] (%)	M_s@300 K (emu cm^{-3})	$T_{c,exp}$ (K)	$T_{c,fit}$ (K)	k_a (100%)	k_d (100%)	(Y + V):Fe[d] (MFC fit)	Y:Fe (XPS)
001_Y-YIG$_1$	10	400	48.9 ± 0.2	81.5 ± 0.4	2.88 ± 0.01	90.00	2.88 ± 0.01	79 ± 4	344	352 ± 5	41.17	19.77	1.23	1.04
001_Y-YIG$_2$	150	300	19.8 ± 0.1	33.0 ± 0.1	2.13 ± 0.01	90.00	2.13 ± 0.01	89 ± 5	390	388 ± 5	32.85	17.40	1.09	1.08
001_Y-YIG$_3$	150	350	40.5 ± 0.2	67.5 ± 0.3	2.57 ± 0.01	90.00	2.57 ± 0.01	76 ± 4	365	362 ± 5	38.99	19.20	1.19	1.03
111_Y-YIG$_1$	10	400	45.0 ± 0.2	125.0 ± 0.6	3.27 ± 0.02	88.76	0.12 ± 0.00	65 ± 3	335	330 ± 5	49.15	17.40	1.29	1.07
111_Y-YIG$_2$	150	300	20.4 ± 0.1	34.0 ± 0.2	2.34 ± 0.01	89.11	0.08 ± 0.00	106 ± 5	398	390 ± 5	35.44	12.53	1.04	1.05
111_Y-YIG$_3$	150	350	40.5 ± 0.2	67.5 ± 0.3	2.73 ± 0.01	88.96	0.10 ± 0.00	84 ± 4	368	362 ± 5	40.43	17.27	1.18	1.09

[a]Out-of-plane lattice spacing compared with that of YIG (lattice parameter 1.237 nm).
[b]Angle between unit cell base vectors.
[c]Volume expansion ratio compared with bulk YIG.
[d]The MFC model cannot distinguish between vacancies (V) and antisite Y on the Fe sites.

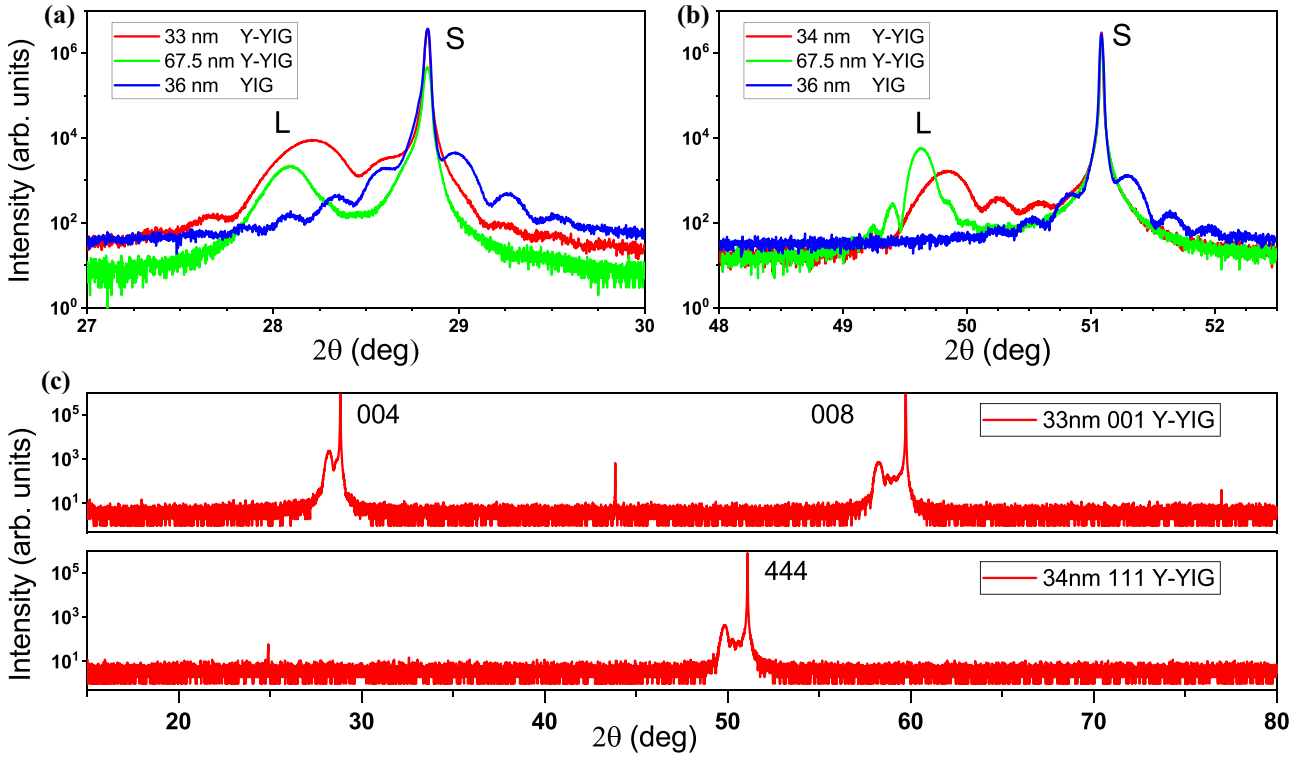

FIG. 1. X-ray diffraction characterization. High resolution x-ray diffraction (HRXRD) 2θ-ω scans of (a) (001) and (b) (111) Y-rich yttrium iron garnet (Y-YIG) samples grown on gadolinium gallium garnet (GGG) substrates. *S* represents the substrate peak, which overlaps the YIG peak, and *L* represents the peak from the Y-YIG films. (c) $2\theta = 15$–80° scan of Y-YIG$_2$ samples with (001) (top) and (111) (bottom) orientations.

For the (001) Y-YIG samples, RSMs of the (408) and (116) peaks were measured to probe the two noncollinear in-plane directions [100] and [110], respectively, whereas for the (111) samples, (642) and (664) peaks were measured to probe [$10\bar{1}$] and [$11\bar{2}$]. Examples are shown in Fig. 2 for 33–34-nm-thick Y-YIG. The RSM shows that films with thickness $t < 150$ nm are fully strained to match the in-plane lattice parameter of the GGG substrate.

These data show that the Y-YIG forms an epitaxial film with a coherent interface on both substrate orientations, without secondary phases. The unit cell of Y-YIG/GGG (001) is tetragonally distorted with $c/a = 1.021$–1.029, whereas the unit cell of Y-YIG/GGG (111) has a rhombohedral distortion along the body diagonal direction with corner angle of 88.8–89.1°. The unit cell dimensions are summarized in Table I. The (001) Y-YIG samples undergo a lattice expansion compared with bulk YIG, but the (111) Y-YIG samples have almost the same unit cell volume as bulk YIG. AFM and XRR characterization (Supplemental Material [34]) shows that the (111) Y-YIG samples have smaller surface roughness than (001) samples.

The Y:Fe ratio was quantified from the XPS spectra of Y 3*d* and Fe 3*p* peaks and normalized by the relative scattering factor. The accuracy of quantification of the Y:Fe ratio is ∼10% [36], and the results of all samples are summarized in the last column of Table I. All films had Y:Fe of 1.04–1.09, i.e., slightly richer in Y than the target composition and significantly greater than the ratio of 0.6 for stoichiometric YIG.

B. DFT calculations

Excess Y in the single-phase garnet films may be incorporated within the structure as antisite defects where Y occupies a Fe site or via the presence of Fe and O vacancies. Prior modeling work [20] indicates that antisite defects Y_{Fe}, Fe_Y and oxygen vacancies V_O have lower formation energies than cation vacancies V_{Fe}, V_Y or Frenkel defects, and Y_{Fe} is therefore likely to be the dominant defect in the Y-YIG. We modeled the magnetic and structural effects of Y_{Fe} by replacing one Fe with one Y in the YIG unit cell [8 f.u., Fig. 3(a)] yielding Y/Fe = 0.641. The results show that the unit cell volume expanded for Y-rich YIG by 0.72% and 0.74% for octahedral ($Y_{Fe,a}$) and tetrahedral ($Y_{Fe,d}$) antisite defects, respectively. Compared with stoichiometric YIG [Fig. 3(b)], Y antisite defects induce structural distortion [Figs. 3(c) and 3(d)]. The Y-O bond length of the dodecahedral site decreases by a small amount near the defect in common for both $Y_{Fe,a}$ and $Y_{Fe,d}$. For $Y_{Fe,a}$, the Fe-O bond length of the O shared with the *d* site is slightly extended, whereas for $Y_{Fe,d}$, the Fe-O bond length for the O shared with the *a* site is slightly contracted. Here, $Y_{Fe,a}$ is more stable than $Y_{Fe,d}$ by 133 meV/f.u., indicating a site preference for Y to occupy the larger octahedral sites, which may be expected from the greater ionic radius of Y^{3+} (110 pm) than Fe^{3+} (65 pm). This differs from prior work [20] which predicted a lower formation energy for $Y_{Fe,d}$ than the $Y_{Fe,a}$.

In stoichiometric YIG, the strongest superexchange coupling is antiferromagnetic between the *d*- and *a*-site Fe^{3+}.

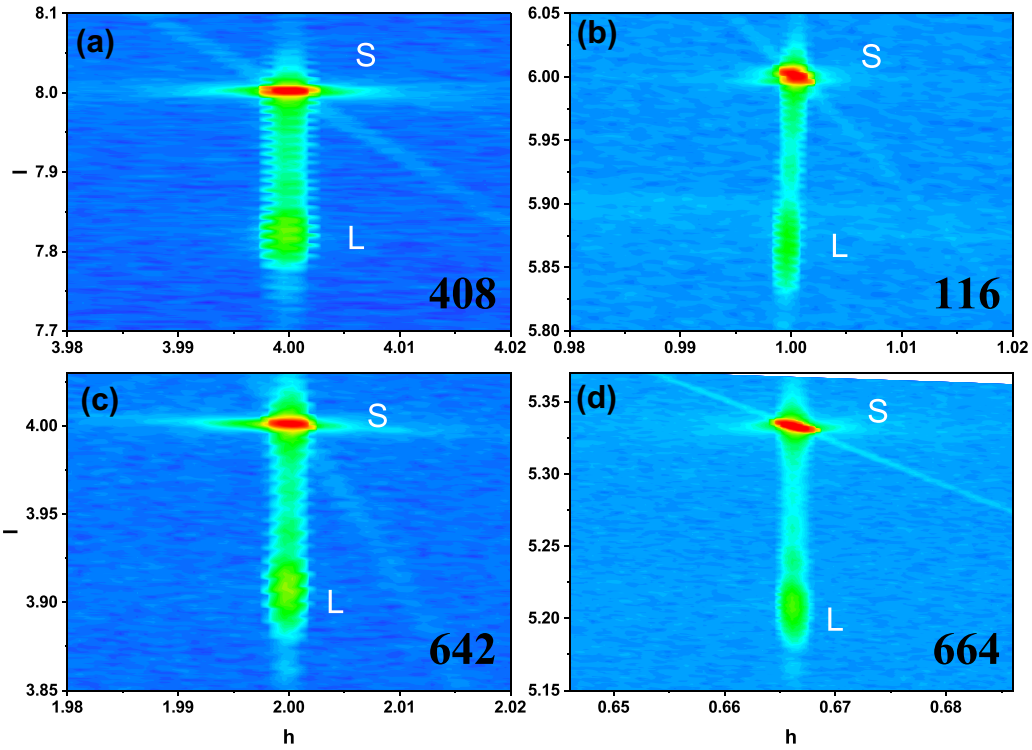

FIG. 2. Reciprocal space mapping (RSM) of Y-rich yttrium iron garnet (Y-YIG) samples. (a) (408) and (b) (116) asymmetric diffraction peaks of 33 nm Y-YIG (001) sample. (c) (642) and (d) (664) asymmetric diffraction peaks of 34 nm Y-YIG (111) sample. Here, $h = q_x d_{mno}$ and $l = q_y d_{pqr}$ are dimensionless reciprocal vectors normalized by the substrate reciprocal lattice parameter, where q_x, q_y are reciprocal vectors of the films and d_{mno}, d_{pqr} are corresponding plane spacings of the substrate [gadolinium gallium garnet (GGG), $a = 12.377$ Å] (e.g., the (408) peak is normalized to d_{001} for h and l; (642) peak to $d_{10\bar{1}}$ for h and d_{111} for l). S represents the substrate and L the film reflection.

With three d-site and two a-site Fe^{3+} per formula unit, the material is ferrimagnetic with a net moment corresponding to one Fe^{3+}, i.e., 5 μ_B/f.u. at low temperatures. Because Y^{3+} has almost zero moment, the antisite Y_{Fe} is equivalent to removing an Fe^{3+} moment, which increases (decreases) the magnetization by 5 μ_B/f.u. when it is in the octahedral (tetrahedral) site. The effect of antisite defects on the magnetism agrees with Ref. [20].

The replacement of Fe^{3+} with Y^{3+} leads to small changes of the Y and O moments as well. Particularly, Y^{3+} in a or d sites has slightly larger moments than Y^{3+} in c sites, and the small moment of $Y_{Fe,a}$ ($Y_{Fe,d}$) is parallel to that of d-site (a-site) Fe^{3+}. Average moments of O increase (decrease) with $Y_{Fe,a}$ ($Y_{Fe,d}$). However, these changes in the Y and O moments are minor, and the main contribution to the magnetization is from the removal of Fe^{3+}.

C. Magnetic properties of Y-YIG

In-plane magnetic hysteresis measurements of Y-YIG samples at different temperatures and fields up to 500 Oe are given in Figs. 4 and 5. The contribution from the paramagnetic GGG substrate is assumed to be linear for $H_{max} < 500$ Oe based on measurements of bare substrates and was subtracted by fitting the slope of the data at fields >200 Oe. The remaining

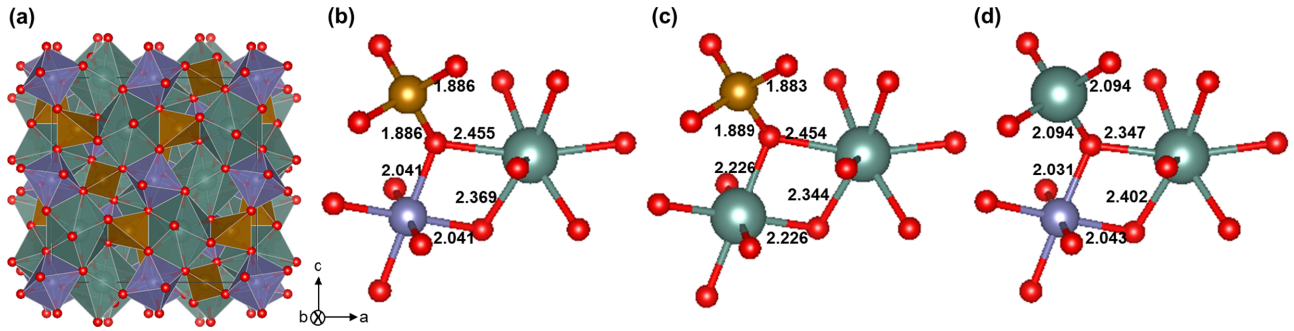

FIG. 3. (a) Unit cell of stoichiometric yttrium iron garnet (YIG). Green, gold, and purple correspond to dodecahedral, tetrahedral, and octahedral sites, respectively. Enlarged structure of YIG with (b) no defects, (c) a $Y_{Fe,a}$ antisite defect, and (d) a $Y_{Fe,d}$ antisite defect. Insets are bond lengths in angstroms.

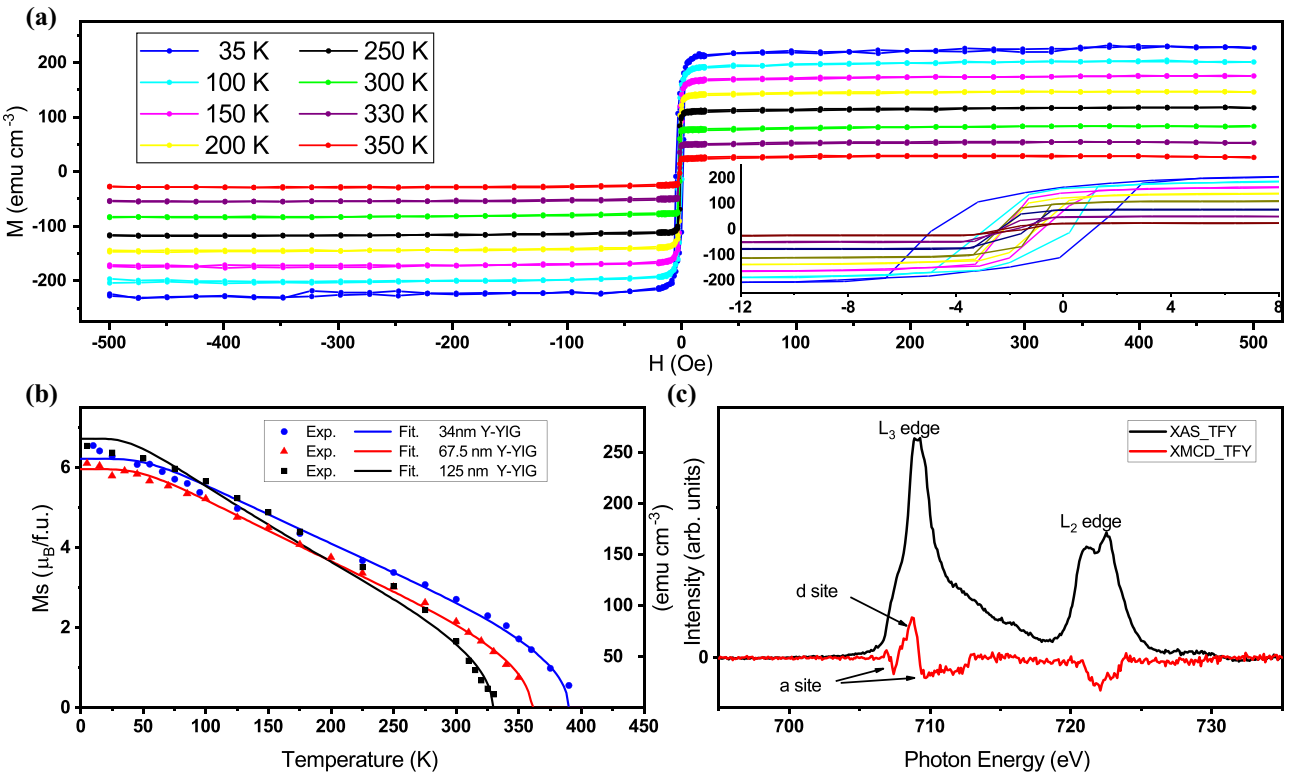

FIG. 4. Magnetic properties and x-ray magnetic circular dichroism (XMCD) measurements of (111) Y-rich yttrium iron garnet (Y-YIG) samples. (a) In-plane hysteresis loops at different temperatures of the 67.5 nm (111) Y-YIG sample. (b) Temperature dependence of saturation magnetization and fitting by Dionne's model for these three samples. (c) XMCD spectra of the 34 nm (111) Y-YIG sample.

magnetization signal normalized by the volume of the Y-YIG is summarized in Fig. 4(a) for a 67.5-nm-thick (111)-oriented sample and Fig. 5(a) for a (001)-oriented sample which was grown simultaneously. At room temperature ($T = 300$ K), the saturation magnetization is $M_{s\_111} = 84\,\mathrm{emu\,cm^{-3}}$ and $M_{s\_001} = 76\,\mathrm{emu\,cm^{-3}}$, which are smaller than that of bulk YIG, $140\,\mathrm{emu\,cm^{-3}}$, or a YIG film of similar thickness ($M_{s\_\mathrm{YIG}} = 137\,\mathrm{emu\,cm^{-3}}$, $t = 79$ nm) [37].

For the (111) Y-YIG sample, the saturation magnetization increases monotonically with decreasing temperature, reaching $240 \pm 12\,\mathrm{emu\,cm^{-3}}$ or $6.5 \pm 0.3\,\mu_B$/f.u.. The coercivity H_c increases at lower temperatures but remains small ($H_c <$ 4 Oe). The 3 Oe offset is attributed to the superconducting magnets [38] and not to an exchange bias. Beaulieu *et al.* [39] also found a monotonic increase in magnetization with decreasing temperature for (111) YIG films. However, for the (001)-oriented Y-YIG samples, the coercivity is much greater, exceeding 100 Oe at 15 K, and the loops become sheared < 70 K, indicative of a change in the reversal mechanism. The saturation magnetization increases with decreasing temperature, but <70 K, the saturation magnetization extracted from the 500 Oe loops starts to decrease. Mitra *et al.* [40] found a decrease in magnetization of (111) YIG films at low temperatures, attributed to antiparallel coupling of a ∼6-nm-thick Gd-rich garnet layer formed by interdiffusion, and Suturin *et al.* [41] showed a ∼10 nm Ga-rich low-moment interdiffused layer in YIG/GGG grown by laser molecular beam epitaxy. However, we believe that the drop in magnetization in our samples has a different origin. The processing conditions used in this paper are like those used to make TmIG/GGG films in Ref. [42], which had an interdiffused layer of only 1 nm thickness. The drop in magnetization occurred only for (001)-oriented Y-YIG films and not for (111)-oriented films, and the decrease was greatest for the thickest film, 001_Y-YIG$_1$, which is inconsistent with an interfacial origin. The drop in magnetization is also larger than that expected from a magnon anomaly proposed by Shamoto *et al.* [43].

We instead attribute the decrease in magnetization of (001)-oriented samples at low temperature to incomplete saturation of the magnetization at the maximum field of the measurement. The field range was limited to 500 Oe to ensure a linear contribution from the substrate: at larger fields ($H > 1000$ Oe) and low temperatures (<25 K), the GGG signal becomes large and nonlinear, which precludes an accurate background subtraction. However, 500 Oe field range is inadequate to saturate the harder (001)-oriented samples at low temperatures (Supplemental Materials [34]), and the magnetization is underestimated as a result. For YIG and presumably Y-YIG, the easy axis is ⟨111⟩, which does not lie in the film plane for either sample orientation. The film is also subject to uniaxial shape anisotropy, a growth-induced anisotropy, and magnetoelastic anisotropy terms. The higher in-plane coercivities fields for (001) Y-YIG than (111) Y-YIG suggest higher magnetic anisotropy or greater pinning of the domain walls during reversal for this orientation.

Antiparallel ordering of the Fe sublattices is confirmed by XMCD measurement of a Y-YIG film, summarized

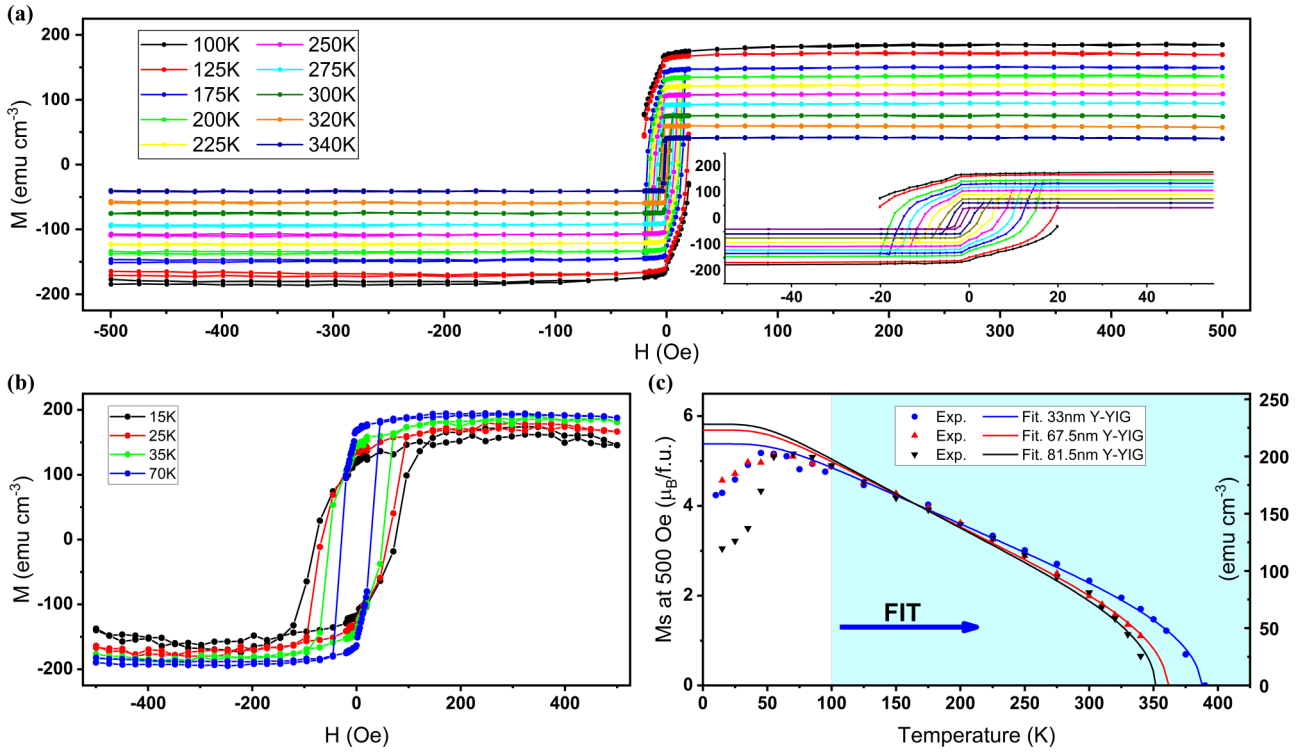

FIG. 5. Magnetic properties of (001) Y-rich yttrium iron garnet (Y-YIG) samples. In-plane hysteresis loops obtained after subtracting linear background signal (a) $T = 100$–340 K and (b) $T = 15$–70 K for the 67.5 nm thick film. (c) Magnetization measured at 500 Oe, and fitting results using Dionne's model for three samples.

in Fig. 4(c). The appearance of two peaks with opposite signs around the shoulders of the main peak at the L_3 absorption edge confirms that the Fe ions occupy two antiparallel sublattices, as found in YIG [44,45]. Therefore, we rewrite the chemical formula of Y-YIG as $\{Y\}_3[Fe_{2\cdot(1-ka)}(Y, V_a)_{2\cdot ka}](Fe_{3\cdot(1-kd)}(Y, V_d)_{3\cdot kd})O_{12}$, where k_a and k_d stand for the fractional substitution by nonmagnetic species Y_{Fe} or vacancies V in the a and d sublattices, with $0 \leqslant k_a, k_d \leqslant 1$. From the higher formation energy of tetrahedral Y_{Fe} vs octahedral Y_{Fe} antisite defects, we expect $k_d \ll k_a$. A preferential a-site Y occupancy is expected to lower the magnetic moment of the octahedral sublattice and increase the low-temperature magnetic moment of Y-YIG compared with that of YIG [3] ($\sim 5\,\mu_B$/f.u.). This is consistent with the extrapolated zero temperature results in Figs. 4(b) and 5(c).

To quantitively analyze the a- and d-site substitution, Dionne's superexchange dilution model [46] combined with Néel's molecular field theory is used to fit the temperature dependence of saturation magnetization [Fig. 4(b)]. The expression for the molecular field coefficients of Y-YIG are adopted from Dionne's work [46] and converted to SI units:

$$\begin{aligned} N_{dd} &= -345.3(1 - 0.87k_a), \\ N_{aa} &= -738.3(1 - 1.26k_d), \\ N_{ad} &= N_{da} = +1101.7(1 - 0.25k_a - 0.38k_d), \end{aligned} \tag{1}$$

where k_a and k_d are the fractional substitutions defined above, and N_{ij} represents the molecular field coefficients between sites i and j.

The magnetization of each sublattice is given by

$$\begin{aligned} M_d(T) &= n_d g_d \mu_B J B_J\left[\frac{\mu_0 m}{k_B T}(N_{dd}M_d + N_{ad}M_a)\right], \\ M_a(T) &= n_a g_a \mu_B J B_J\left[\frac{\mu_0 m}{k_B T}(N_{da}M_d + N_{aa}M_a)\right], \\ M(T) &= |M_d - M_a|, \end{aligned} \tag{2}$$

where n_i is the volume density of Fe^{3+} of the a and d sublattices, $g_a = g_d = 2$ is the Landé factor, and B_J is the Brillouin function ($J = L + S = 0 + \frac{5}{2} = \frac{5}{2}$).

Using a nonlinear least square fitting algorithm from MATLAB, k_a and k_d values were obtained by fitting Dionne's model to the experimental data, and the results are summarized in Table I. Figure 4(b) shows the fitting of (111)-oriented Y-YIG samples grown at different conditions. For the (001)-oriented samples, the fit is carried out for the temperature range of 100–400 K, and the results are shown in Fig. 5(c).

The (Y + Fe):Fe ratio of Y-YIG samples can be calculated by substituting the fitted k_a and k_d values into the chemical formula $\{Y\}_3[Fe_{2\cdot(1-ka)}(Y, V_a)_{2\cdot ka}](Fe_{3\cdot(1-kd)}(Y, V_d)_{3\cdot kd})O_{12}$ and is shown in Table I. The vacancies and Y antisite defects cannot be distinguished by the model. In the case of no vacancies, $Y : Fe = (3 + 2k_a + 3k_d)/(5 - 2k_a - 3k_d)$. For the samples Y-YIG$_2$ grown at 300 mJ laser energy and 150 mTorr oxygen, corresponding to a low growth rate, the (Y + V):Fe atomic ratios calculated from the fit, 1.04 for (111)-oriented and 1.09 for (100)-oriented films, agree very well with Y:Fe determined from XPS, 1.05 and 1.08, respectively, and are like the target stoichiometry of 1.00. This suggests that there

is a negligible population of V_a and V_d, and the excess Y is accommodated in the Fe sites.

For the Y-YIG$_1$ and Y-YIG$_3$ grown samples grown with lower O_2 or higher laser power corresponding to a higher growth rate, the Y:Fe ratio from XPS remains at 1.03–1.09, whereas (Y + V):Fe has a value of ∼1.2–1.3. This indicates a more complex site occupancy. Table S3 in the Supplemental Material [34] shows the vacancy concentration estimated from the data, which ranges from 0.32 to 0.77 out of the five total a and d sites, though the individual occupancy of Y and V_{Fe} on each site cannot be separately determined. Here, V_{Fe} implies the additional presence of oxygen vacancies or higher valence Fe for charge balance. These defects may also modify the parameters in the superexchange model, for example, weakening the ferrimagnetic coupling and lowering the Curie temperature beyond the effects of the nonmagnetic substituents. We speculate that the greater amount of V_{Fe} proposed to exist in samples Y-YIG$_1$ and Y-YIG$_3$ is due to their faster growth rate, though a more systematic study of deposition conditions would be required to verify this.

Accommodation of Y only on the octahedral sites would imply $k_a = 0.55$ and $k_d = 0$ for a net composition of Y : Fe = 1.05. Considering the Y-YIG$_2$ samples, the fit gave $k_a = 0.35$ and 0.33 and $k_d = 0.13$ and 0.17 for the (111)- and (100)-oriented samples, respectively. This indicates that the $Y_{Fe,a}$ antisite dominates, but there is also a large fraction of tetrahedral $Y_{Fe,d}$ antisite defects. The other samples also showed large amounts of $Y_{Fe,d}$. The large fraction of $Y_{Fe,d}$ may be surprising, given the small size of the tetrahedral site, but the structure can distort, and DFT showed that the $Y_{Fe,d}$ antisites are only modestly unfavorable compared with the $Y_{Fe,a}$ antisites. Based on the energy difference of 0.113 eV at equilibrium, at the growth temperature, we would expect ∼25% of the Y_{Fe} to be in tetrahedral sites. A consequence of the presence of $Y_{Fe,d}$ as well as $Y_{Fe,a}$ is the value of the low-temperature saturation magnetization, which extrapolates to 6–6.5 μ_B/f.u. for the (111) and 5.5 μ_B/f.u. for the (001)-oriented Y-YIG films. This is larger than that of YIG (5 μ_B/f.u.) but smaller than the value expected for complete octahedral substitution of the excess Y, ∼10 μ_B/f.u.

The Curie temperature of the Y-YIG samples was determined by empirical interpolation for $T > 150$ K based on Bloch's law: $M = M_0[1 - (T/T_c)^\gamma]^\delta$ yielding a value of $T_{c,exp}$ and also from Dionne's superexchange model yielding a value $T_{c,fit}$ at $M = 0$. The results are summarized in Table I and show that the two methods agree to within 8 K. (Table S1 in the Supplemental Material [34] shows the Bloch law fit for the additional samples). Compared with YIG [47] ($T_c = 559$ K), the Curie temperature of Y-YIG is considerably lower by 170–200 K. The Y substitution on both a and d sites lowers the density of Fe-O-Fe bonds and therefore weakens the intrasublattice (within a and d) and intersublattice (between a and d) exchange coupling, causing a drop in Curie temperature. The Curie temperature of bulk $Y_3[In_{0.5}Fe_{1.5}](Fe_3)O_{12}$ and $Y_3[Sc_{0.75}Fe_{1.25}](Fe_3)O_{12}$ reported by Gilleo and Geller [3] is ∼480 and 420 K, respectively, and the greater substitution for $Y_3[YFe](Fe_3)O_{12}$ implies that the Curie temperature should be even lower, which agrees with our observations. The Curie temperature of Y-YIG samples is lowest for the higher growth rate samples, which is consistent with the possible presence of larger amounts of other defects such as vacancies.

The structural and magnetic results show that epitaxially grown garnet can accommodate a large nonideality in the Y:Fe ratio that would drive formation of other phases (i.e., the perovskite $YFeO_3$) in a bulk material or one not stabilized by epitaxy. Despite the size difference between Y^{3+} and Fe^{3+}, the data support the incorporation of excess Y by the formation of Y_{Fe} antisite defects. This occurs for both a and d sites, though with a greater fraction of a-site Y_{Fe}, leading to increased low-temperature saturation magnetization compared with that of YIG. The presence of Y_{Fe} and potentially other defects, especially in high growth rate films, lowers the Curie temperature to 340–390 K, and the room temperature magnetization of Y-YIG is smaller than that of YIG. Excess Y therefore behaves like other nonmagnetic substituents with an octahedral site preference. The formation of the Y-YIG nonequilibrium phase using PLD with epitaxial stabilization leads to properties that are not found in bulk garnets, and this strategy may also be extended to other thin film garnet compositions.

IV. SUMMARY

Y-substituted YIG with a Y:Fe ratio ∼1:1 was epitaxially grown on GGG substrates using PLD. There was no evidence of secondary phases, and x-ray diffraction revealed that the films have high structural quality but that the unit cell underwent tetragonal and rhombohedral distortion for (001)- and (111)-oriented substrates, respectively. Compared with stoichiometric YIG, the Curie temperature of Y-YIG is much lower, $T_c = 330$–390 K, and is sensitive to the growth conditions, and the low-temperature saturation magnetization of the Y-YIG is higher than that of YIG. The structural and magnetic data indicate that the excess Y is accommodated as antisite defects on the Fe sites. The fitting of the temperature-dependent magnetization by a superexchange model indicates that Y_{Fe} preferentially occupies the octahedral site, as expected from its lower formation energy, but there is a significant amount of tetrahedral Y_{Fe}, and in some cases, V_{Fe} are also likely to be present. The excess Y modifies the magnetic properties of YIG in a manner that resembles that of other nonmagnetic substituents with a preference for the a sites. The key difference is that, for a Y:Fe ratio ∼ 1:1, the perovskite $YFeO_3$ is the thermodynamically stable phase rather than the garnet $Y_3[YFe](Fe_3)O_{12}$, and Y-YIG is only formed due to its epitaxial stabilization on a garnet substrate. We may similarly expect that other rare earth garnets $R_{3+x}Fe_{5-x}O_{12}$ could be grown with a large excess of rare earth, opening a range of interesting properties not found in bulk garnets.

ACKNOWLEDGMENTS

The authors are grateful to Dr. Richard Rosenberg, Jackson Bauer, and Ethan Rosenberg for their help on x-ray absorption spectroscopy and XMCD measurements. The authors gratefully acknowledge support from National Science Foundation Awards No. DMR 1911792 and No. DMR 1419807, Spintronic Materials for Advanced Information Technologies, an nCORE Center of the Semiconductor Research Corporation, the Defense Advanced Research Projects Agency, and the

use of Materials Research Science and Engineering Centers shared facilities under No. DMR 1419807. EC acknowledges support from a Kwanjeong Fellowship. This paper also used resources of the Advanced Photon Source, a U.S. Department of Energy (DOE) Office of Science User Facility operated for the DOE Office of Science by Argonne National Laboratory under Contact No. DE-AC02-06CH11357.

[1] S. Geller and M. A. Gilleo, Structure and ferrimagnetism of yttrium and rare-earth-iron garnets, Acta Crystallogr. **10**, 239 (1957).

[2] J. W. Nielsen and E. F. Dearborn, The growth of single crystals of magnetic garnets, J. Phys. Chem. Solids **5**, 202 (1958).

[3] M. A. Gilleo and S. Geller, Magnetic and crystallographic properties of substituted yttrium-iron garnet, $3Y_2O_3 \cdot xM_2O_3 \cdot (5-x)Fe_2O_3$, Phys. Rev. **110**, 73 (1958).

[4] M. A. Gilleo and S. Geller, Substitution for iron in ferrimagnetic yttrium-iron garnet, J. Appl. Phys. **29**, 380 (1958).

[5] S. Geller, H. J. Williams, R. C. Sherwood, and G. P. Espinosa, Substitutions of divalent transition metal ions in yttrium iron garnet, J. Appl. Phys. **33**, 1195 (1962).

[6] S. Geller, H. J. Williams, R. C. Sherwood, and G. P. Espinosa, Substitutions of divalent manganese, iron and nickel in yttrium iron garnet, J. Phys. Chem. Solids **23**, 1525 (1962).

[7] V. Sharma and B. K. Kuanr, Magnetic and crystallographic properties of rare-earth substituted yttrium-iron garnet, J. Alloys Compd. **748**, 591 (2018).

[8] M. S. Lataifeh, Room temperature magnetization measurements of some substituted rare earth iron garnets, Appl. Phys. A **92**, 681 (2008).

[9] T. Sekijima, H. Kishlmoto, T. Fujii, K. Waking, and M. Okada, Magnetic, optical and microwave properties of rare-earth-substituted fibrous yttrium iron garnet single crystals grown by floating zone method, Jpn. J. Appl. Phys. **38**, 5874 (1999).

[10] H. Uchida, Y. Masuda, R. Fujikawa, A. V. Baryshev, and M. Inoue, Large enhancement of Faraday rotation by localized surface plasmon resonance in Au nanoparticles embedded in Bi:YIG film, J. Magn. Magn. Mater. **321**, 843 (2009).

[11] V. Berzhansky, T. Mikhailova, A. Shaposhnikov, A. Prokopov, A. Karavainikov, V. Kotov, D. Balabanov, and V. Burkov, Magneto-optics of nanoscale Bi:YIG films, Appl. Opt. **52**, 6599 (2013).

[12] A. N. Shaposhnikov, A. R. Prokopov, A. V. Karavainikov, V. N. Berzhansky, T. V. Mikhailova, V. A. Kotov, D. E. Balabanov, I. V. Sharay, O. Y. Salyuk, M. Vasiliev, and V. O. Golub, Modification of Bi:YIG film properties by substrate surface ion pre-treatment, Mater. Res. Bull. **55**, 19 (2014).

[13] T. Fakhrul, S. Tazlaru, L. Beran, Y. Zhang, M. Veis, and C. A. Ross, Magneto-optical Bi:YIG films with high figure of merit for nonreciprocal photonics, Adv. Opt. Mater. **7**, 1900056 (2019).

[14] A. D. Block, P. Dulal, B. J. H. Stadler, and N. C. A. Seaton, Growth parameters of fully crystallized YIG, Bi:YIG, and Ce:YIG films with high Faraday rotations, IEEE Photonics J. **6**, 1 (2014).

[15] H. S. Yoder and M. L. Keith, Complete substitution of aluminum for silicon: the system $3MnO \cdot Al_2O_3 \cdot 3SiO_2 - 3Y_2O_3 \cdot 5Al_2O_3$, Am. Mineral. **36**, 519 (1951).

[16] J. R. Cunningham and E. E. Anderson, Samarium substitutions in yttrium iron garnet, J. Appl. Phys. **31**, S45 (1960).

[17] A. Nakatsuka, A. Yoshiasa, and S. Takeno, Site preference of cations and structural variation in $Y_3Fe_{5-x}Ga_xO_{12}$ ($0 \leqslant x \leqslant 5$) solid solutions with garnet structure, Acta Crystallogr. Sect. B **51**, 737 (1995).

[18] J. R. Cunningham and E. E. Anderson, Effect of indium substitution in yttrium iron garnet. High permeability garnets, J. Appl. Phys. **32**, S388 (1961).

[19] G. P. Espinosa, A crystal chemical study of titanium(IV) and chromium(III) substituted yttrium iron and gallium garnets, Inorg. Chem. **3**, 848 (1964).

[20] S. Tan, W. Zhang, L. Yang, J. Chen, and Z. Wang, Intrinsic defects in yttrium iron garnet: a first-principles study, J. Appl. Phys. **128**, 183904 (2020).

[21] P. Perrot, *Iron–Oxygen–Yttrium: Datasheet from Landolt-Börnstein - Group IV Physical Chemistry*, Ternary Alloy Systems in Springer Materials, Vol. 11D5 (Springer-Verlag, Berlin, Heidelberg, 2009), 3261.

[22] H. J. van Hook, Phase relations in the system Fe_2O_3–Fe_3O_4–$YFeO_3$ in air, J. Am. Ceram. Soc. **44**, 208 (1961).

[23] A. P. Galayda, N. E. Volkova, L. Y. Gavrilova, K. G. Balymov, and V. A. Cherepanov, Phase equilibria, structure and properties of intermediate phases in the Sm_2O_3–Fe_2O_3–CoO and Sm_2O_3–CaO–CoO systems, J. Alloys Compd. **718**, 288 (2017).

[24] Y. D. Tretyakov, V. V. Sorokin, A. R. Kaul, and A. P. Erastova, Phase equilibria and thermodynamics of coexisting phases in rare-earth element-iron-oxygen systems. I. The cerium-iron-oxygen system, J. Solid State Chem. **18**, 253 (1976).

[25] S. A. Manuilov, S. I. Khartsev, and A. M. Grishin, Pulsed laser deposited $Y_3Fe_5O_{12}$ films: nature of magnetic anisotropy I, J. Appl. Phys. **106**, 123917 (2009).

[26] S. A. Manuilov and A. M. Grishin, Pulsed laser deposited $Y_3Fe_5O_{12}$ films: nature of magnetic anisotropy II, J. Appl. Phys. **108**, 013902 (2010).

[27] M. Lahoubi, Symmetry analysis of the magnetic structures in TbIG and Tb:YIG at low temperature, J. Phys. Conf. Ser. **340**, 12068 (2012).

[28] Y. Dumont, N. Keller, E. Popova, D. S. Schmool, S. Bhattacharya, B. Stahl, M. Tessier, and M. Guyot, Superexchange and iron valence control by off-stoichiometry in yttrium iron garnet thin films grown by pulsed laser deposition, J. Appl. Phys. **97**, 10G108 (2005).

[29] W. Noun, E. Popova, F. Bardelli, Y. Dumont, R. Bertacco, A. Tagliaferri, M. Tessier, M. Guyot, B. Berini, and N. Keller, Determination of yttrium iron garnet superexchange parameters as a function of oxygen and cation stoichiometry, Phys. Rev. B **81**, 054411 (2010).

[30] Y. Dumont, N. Keller, E. Popova, D. S. Schmool, M. Tessier, S. Bhattacharya, B. Stahl, R. M. C. Da Silva, and M. Guyot, Tuning magnetic properties with off-stoichiometry in oxide thin films: An experiment with yttrium iron garnet as a model system, Phys. Rev. B **76**, 104413 (2007).

[31] B. Vertruyen, R. Cloots, J. S. Abell, T. J. Jackson, R. C. da Silva, E. Popova, and N. Keller, Curie temperature, exchange integrals, and magneto-optical properties in off-stoichiometric bismuth iron garnet epitaxial films, Phys. Rev. B **78**, 094429 (2008).

[32] V. Chlan, H. Sˇtěpánková, V. Procházka, J. Englich, J. Kohout, D. Nizˇňanský, and J. Bursˇík, Antisite defects in lutetium and yttrium iron garnets prepared by liquid mix technique, J. Magn. Magn. Mater. **290–291**, 993 (2005).

[33] J. L. MacManus-Driscoll, M. P. Wells, C. Yun, J.-W. Lee, C.-B. Eom, and D. G. Schlom, New approaches for achieving more perfect transition metal oxide thin films, APL Mater. **8**, 40904 (2020).

[34] See Supplemental Material at http://link.aps.org/supplemental/10.1103/PhysRevMaterials.5.094403 for additional information on growth condition, structure, XRR, AFM, and XPS quantification of Y-YIG samples; DFT calculation, Dionne's superexchange dilution model MATLAB code, and data fitting; vacancy calculation and low-temperature magnetometry of Y-YIG.

[35] K. Momma and F. Izumi, VESTA 3 for three-dimensional visualization of crystal, volumetric and morphology data, J. Appl. Crystallogr. **44**, 1272 (2011).

[36] S. Tougaard, Accuracy of the non-destructive surface nanostructure quantification technique based on analysis of the XPS or AES peak shape, Surf. Interface Anal. **26**, 249 (1998).

[37] M. C. Onbasli, A. Kehlberger, D. H. Kim, G. Jakob, M. Kläui, A. V. Chumak, B. Hillebrands, and C. A. Ross, Pulsed laser deposition of epitaxial yttrium iron garnet films with low Gilbert damping and bulk-like magnetization, APL Mater. **2**, 106102 (2014).

[38] M. Buchner, K. Höfler, B. Henne, V. Ney, and A. Ney, Tutorial: basic principles, limits of detection, and pitfalls of highly sensitive SQUID magnetometry for nanomagnetism and spintronics, J. Appl. Phys. **124**, 161101 (2018).

[39] N. Beaulieu, N. Kervarec, N. Thiery, O. Klein, V. Naletov, H. Hurdequint, G. de Loubens, J. Ben Youssef, and N. Vukadinovic, Temperature dependence of magnetic properties of a ultrathin yttrium-iron garnet film grown by liquid phase epitaxy: effect of a Pt overlayer, IEEE Magn. Lett. **9**, 1 (2018).

[40] A. Mitra, O. Cespedes, Q. Ramasse, M. Ali, S. Marmion, M. Ward, R. M. D. Brydson, C. J. Kinane, J. F. K. Cooper, S. Langridge, and B. J. Hickey, Interfacial origin of the magnetisation suppression of thin film yttrium iron garnet, Sci. Rep. **7**, 11774 (2017).

[41] S. M. Suturin, A. M. Korovin, V. E. Bursian, L. V. Lutsev, V. Bourobina, N. L. Yakovlev, M. Montecchi, L. Pasquali, V. Ukleev, A. Vorobiev, A. Devishvili, and N. S. Sokolov, Role of gallium diffusion in the formation of a magnetically dead layer at the $Y_3Fe_5O_{12}/Gd_3Ga_5O_{12}$ epitaxial interface, Phys. Rev. Mater. **2**, 104404 (2018).

[42] L. Caretta, E. Rosenberg, F. Büttner, T. Fakhrul, P. Gargiani, M. Valvidares, Z. Chen, P. Reddy, D. A. Muller, C. A. Ross, and G. S. D. Beach, Interfacial Dzyaloshinskii-Moriya interaction arising from rare-earth orbital magnetism in insulating magnetic oxides, Nat. Commun. **11**, 1090 (2020).

[43] S.-i. Shamoto, Y. Yasui, M. Matsuura, M. Akatsu, Y. Kobayashi, Y. Nemoto, and J. Ieda, Ultralow-energy magnon anomaly in yttrium iron garnet, Phys. Rev. Res. **2**, 033235 (2020).

[44] Y. Y. Chin, H.-J. Lin, Y.-F. Liao, W. C. Wang, P. Wang, D. Wu, A. Singh, H.-Y. Huang, Y.-Y. Chu, D. J. Huang, K.-D. Tsuei, C. T. Chen, A. Tanaka, and A. Chainani, Local spin moments, valency, and long-range magnetic order in monocrystalline and ultrathin films of $Y_3Fe_5O_{12}$ garnet, Phys. Rev. B **99**, 184407 (2019).

[45] H. B. Vasili, B. Casals, R. Cichelero, F. Macià, J. Geshev, P. Gargiani, M. Valvidares, J. Herrero-Martin, E. Pellegrin, J. Fontcuberta, and G. Herranz, Direct observation of multivalent states and $4f \rightarrow 3d$ charge transfer in Ce-doped yttrium iron garnet thin films, Phys. Rev. B **96**, 014433 (2017).

[46] G. F. Dionne, Molecular field coefficients of substituted yttrium iron garnets, J. Appl. Phys. **41**, 4874 (1970).

[47] E. E. Anderson, Molecular field model and the magnetization of YIG, Phys. Rev. **134**, A1581 (1964).